GEOPHYSICS

Discovery of distinct lithosphere-asthenosphere boundary and the Gutenberg discontinuity in the Atlantic Ocean

Pranav Audhkhasi† and Satish C. Singh*

The plate tectonic theory requires a rigid lithosphere floating over a weak asthenosphere, separated by the lithosphere-asthenosphere boundary, which has been sometimes interpreted as the Gutenberg discontinuity. Using a deep seismic reflection technique, we report the presence of two continuous reflections covering 27 Ma to 58 Ma oceanic lithosphere in the Atlantic Ocean. We find that the upper reflection deepens with age and follows the ~1250°C isotherm, whereas the deeper reflection lies at a constant depth of ~75 km. We suggest that the upper reflection represents the thermally controlled lithosphere-asthenosphere boundary, whereas the lower reflection is the Gutenberg discontinuity, a frozen-in dehydration boundary separating the dry mantle melting region above from the hydrated mantle below formed at the ridge axis. We also find that thermal mantle anomalies rejuvenate the lithosphere, uplift the lithosphere-asthenosphere boundary, and destroy the Gutenberg discontinuity.

INTRODUCTION

The plate tectonics theory is based on the concept of a rigid lithospheric plate floating over a weak, deformable, and convecting asthenosphere, separated by a boundary termed as the lithosphere-asthenosphere boundary (LAB). Determining the depth and nature of the LAB is fundamental for understanding the formation and evolution of the oceanic lithosphere, and the associated plate tectonic processes. Thermal modeling studies indicate that the LAB should be shallow near the ridge axis and deepen with age as the plate cools and subsides (1). Surface wave tomography studies have shown the presence of a high shear wave velocity lid associated with the lithosphere, which decreases smoothly to a low velocity in the asthenosphere (2). The LAB has been defined either by a maximum negative velocity gradient (3) or at a constant shear wave velocity contour of 4.4 km/s (4). These results, however, indicate that the lithospheric lid thickens with age, consistent with thermal models. On the other hand, anisotropy (3) and some scattering studies (5, 6) have indicated that the LAB lies at a constant depth of 60 to 80 km and does not vary with age, which has sometimes been interpreted as the Gutenberg (G) discontinuity (7), but the relationship between the LAB and the G-discontinuity remains a matter of debate (8, 9). Since the resolution of passive seismic methods is very low, 10 to 30 km vertically and 50 to 200 km laterally (10), it is rather difficult to distinguish between LAB and G-discontinuity, and hence, different competing models have been proposed for their origins (8, 11).

Recently, active source seismic reflection methods have provided high-resolution images (500 m vertically and 1 to 5 km horizontally) of the LAB (12, 13), showing that the LAB is bounded by two reflections, top and bottom, and the LAB possibly consists of a thick melt channel. However, these studies have been limited to only a few discrete ages, namely, 40 million years (Ma), 70 Ma, and 120 Ma,

and hence, they do not provide information about the evolution of the LAB with age and its relationship with the G-discontinuity. Here, we present high-resolution seismic reflection images of the LAB system continuously on a hundred meter to a kilometer scale over 1.8-Ma to 75.6-Ma oceanic lithosphere in the equatorial Atlantic Ocean, offering unprecedented details in the variation of the LAB, allowing to distinguish between LAB and G-discontinuity and propose models for their formations and evolutions.

Our study region lies in the equatorial Atlantic Ocean on the African Plate over the lithosphere formed at the Mid-Atlantic Ridge (MAR) between the Chain fracture zone in the north and the Ascension fracture zone in the south (Fig. 1). This ~700-km-long segment of the MAR is disrupted by only short offset transform faults and nontransform offsets (fig. S1) and hence offers an ideal environment to study the thermal evolution of a normal oceanic lithosphere continuously over a large age range. The half spreading rate in this area has varied between 8 and 25 mm/year (fig. S2), with an average of ~20 mm/year (14).

In the southeast part of our study area, two prominent volcanic chains are present, the St. Helena volcanic chain and the Cameroon Volcanic Line (CVL), which can be distinguished by their ages of the volcanic islands (Fig. 1). The St. Helena volcanic chain is a northeast-southwest (NE-SW) trending chain of seamounts in a ~500-km-wide zone. The ages of the volcanic outcrops of the St. Helena chain vary from ~80 Ma in the NE (Fig. 1) to ~52 Ma in the SE (15), ~20 Ma younger than the surrounding seafloor ages (14). Further NE, the ~1600-km-long N30E trending CVL extends up to ~600 km over the oceanic lithosphere (Fig. 1). The volcanism seemed to have started in the oceanic domain 30 Ma ago on the Principe Island with the youngest rocks (1 Ma old) found on the Sao Tome and Annobon Islands (16). The passage of these hotspots could introduce chemical heterogeneities (17) in the lithosphere and possibly modify the thermal regime in the region.

RESULTS

In 2015, we acquired a ~1400-km-long seismic reflection profile in international waters covering the oceanic lithosphere of 1.8 Ma to

Institut de Physique du Globe de Paris, Université de Paris Cité, 1 Rue Jussieu, 75005 Paris, France.
*Corresponding author. Email: singh@ipgp.fr
†Present address: Norges Teknisk-Naturvitenskapelige Universitet (NTNU), Høgskoleringen 1, 7491 Trondheim, Norway.
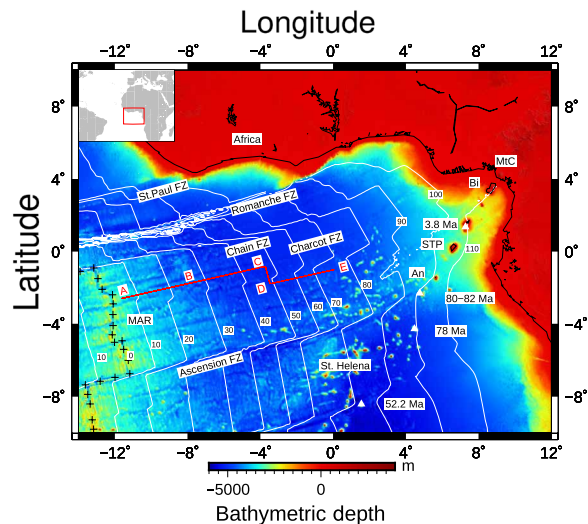
Fig. 1. Study region. The bathymetry map of the study region (*14*) in the equatorial Atlantic Ocean along with the seafloor ages (*14*) in white contours and the multi-channel seismic profile in red. Prominent features such as fracture zones (FZ) and volcanic chains have been marked. Segments A-C (2 Ma to 47 Ma) and D-E (49 Ma to 75 Ma) denote the flowlines, and segment C-D (47 Ma to 49 Ma) denotes the isochrone line along the profile, with point B marking the change of recording parameters. White triangles denote the volcanic outcrops of the St. Helena chain and Cameroon Volcanic Line (CVL) and their estimated ages (*14*, *15*). The seafloor age and half-spreading rate (*14*) along the profile are given in fig. S2, and the second-order discontinuities are better visualized using vertical gravity gradient (fig. S1). The CVL comprises four main volcanic outcrops: Mount Cameroon (MtC), Bioko (Bi), Sao Tome and Principe (STP), and Annobon (An). MAR, Mid-Atlantic Ridge.

75.6 Ma (Fig. 1 and figs. S1 and S2). The entire profile is divided into two flowlines denoted by A-C and D-E and one connecting isochrone line denoted by C-D. The flowline A-C spans an age range of ~2 Ma to 47 Ma and D-E from ~49 Ma to 75 Ma. The isochrone line is 107 km long and crosses two second-order discontinuities (SODs) (Fig. 1 and fig. S1) and covers an approximate age from 47 Ma to 49 Ma. The final composite seismic P-wave reflection image in two-way travel time (TWTT) for the entire profile is shown in Fig. 2 (see Materials and Methods for data acquisition and processing and figs. S3 to S15). The blow-up of the seismic images can be found in figs. S17 to S19.

We observe the Moho reflection to be intermittently imaged along the profile approximately at 1- to 3-s TWTT below the seafloor (bsf) (cyan arrows in Fig. 2). We also observe two prominent mantle reflections along the whole profile (red and green arrows in Fig. 2). The Fresnel zone widths at depths of imaged mantle reflections are 1.5 to 3.5 times larger than that at the Moho depth, allowing an enhanced lateral continuity at the depths of the mantle reflections.

The rough seafloor formed at a slow spreading ridge is devoid of sediment cover at young ages (Fig. 2 and fig. S17), which scatters energy, making it difficult to image structures underneath. Several small events can be observed in the mantle below the Moho (Fig. 2 and fig. S17), but we observe one weak dipping reflection event starting at 11.7 s at zero distance to 19.2 s at 220-km distance (red arrows in Fig. 2) that could be interpreted as the base of the lithosphere. The reflection time of this upper reflection exceeds 20-s TWTT beyond 20 Ma (300-km distance in Fig. 2), and hence, we do

not have any constraint on it between 16 Ma and 27 Ma (point B). With the increasing age, the sediment cover thickens and reduces the scattering effect of the rough seafloor, improving the imaging conditions. At 27 Ma (point B in Fig. 2 and fig. S18), the upper reflection can be followed at ~22 s, which continues to dip toward older ages up to ~26 s at 47 Ma. On the isochrone line C-D, this upper reflection shallows with age to 23.5 s at 49 Ma (Fig. 2 and fig. S19) and then continues dipping toward older age up to 27 s at 75 Ma (point E in Fig. 2 and fig. S19). Another gently dipping lower reflection is observed at ~27.5 s at 27 Ma (Fig. 2 and fig. S18) and continues until ~28 s at 47 Ma (point C in Fig. 2 and fig. S18). This lower reflection can be followed up to ~1120 km (58 Ma) along the profile down to 29 s (Fig. 2 and fig. S19).

DISCUSSION

Nature of deep mantle seismic reflections

These reflections are caused by subsurface structures as they are neither associated with water reverberations (multiples; fig. S16) nor due to sideswipes originating from seafloor features, as we do not observe any seafloor features that extend more than 1400 km. Although a localized visual analysis (figs. S17 to S19) of the waveforms of these reflections shows mixed polarities, statistical analyses of the polarities (see Materials and Methods and fig. S20) suggest that the two reflections have predominantly negative polarities with respect to that of the seafloor, suggesting that there is a high probability (>50%) that these reflections are produced by a decrease in velocity contrasts. The analysis of the amplitudes of the upper reflection (see Materials and Methods and fig. S21A) with respect to the seafloor reflections suggests that there is a 5.9 ± 0.6% decrease in the P-velocity across it. On the basis of the continuity of the upper reflection over >1000 km (Fig. 2 and figs. S17 to S19), its deepening toward the older oceanic lithosphere, and the negative P-velocity contrast, we interpret the upper reflection as the base of the lithosphere, LAB. The lower reflection shows a further 5 ± 0.6% decrease in the P-velocity (figs. S20 and S21B) and could be either the base of a melt channel (*13*) or the G-discontinuity (*5*). The synthetic seismogram modeling study indicates that these reflections could be produced by either steps in velocities or by thin low-velocity layers, around 500 to 750 m thick (see Materials and Methods and fig. S22).

LAB reflection

We picked the two mantle reflections and depth-converted them using a two-dimensional (2D) velocity (fig. S23), taking the crustal and upper mantle P-velocities from a colocated wide-angle tomography study (see Materials and Methods), and the depth-converted image is shown in Fig. 3. We found that a substantial part of the upper reflection, interpreted as the LAB reflection, follows the 1250 ± 20°C isotherm of the plate-cooling model (Fig. 3 and fig. S25) (*1*). For younger ages (<5 Ma), the LAB reflection is nearly flat at 16- to 18-km-depth bsf and it does not follow any isotherms (Fig. 3). The flatness of the reflection and the mismatch with the isotherms could be due to the fact that the thermal models do not consider the effects of hydrothermal circulation that would affect the lithosphere at younger ages and flatten the isotherms (*18*). Beyond ~5 Ma, the LAB reflection starts dipping steeply until almost ~12 Ma with a slope of 2.5 km/Ma (fig. S24), where it reaches to a depth of ~35-km bsf (Fig. 3). This steepening could be associated with a thermal edge effect induced by the mantle melt cone beneath
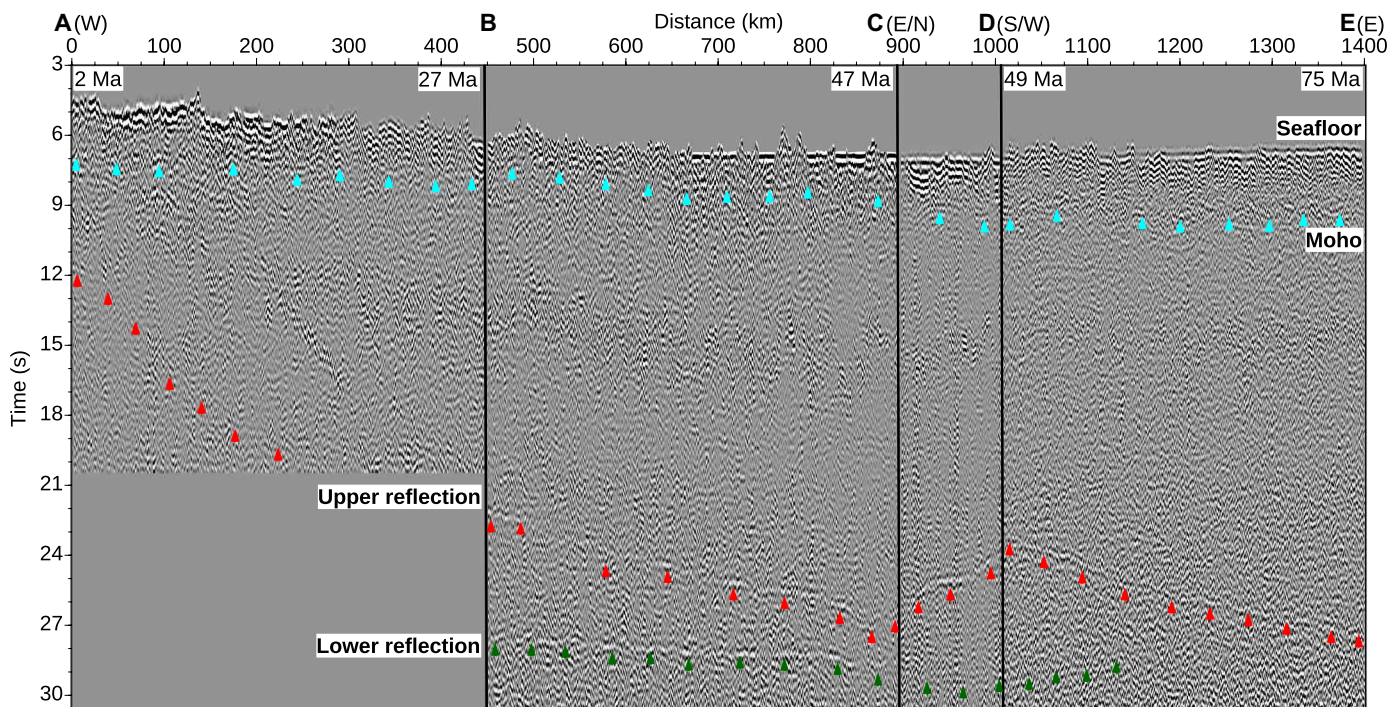
Fig. 2. Seismic reflection image in the time domain. Final seismic image in TWTT along the profile after extensive processing (see figs. S3 to S15 and Materials and Methods). The segment boundaries along the profile (Fig. 1) are demarcated by solid black vertical lines at points B (27 Ma), C (47 Ma), and D (49 Ma). The seafloor, Moho (cyan arrows), and upper (red) and lower (green) mantle reflections have been marked. The blow-ups of the individual segments A-B, B-C, and C-E are shown in figs. S17, S18, and S19, respectively.
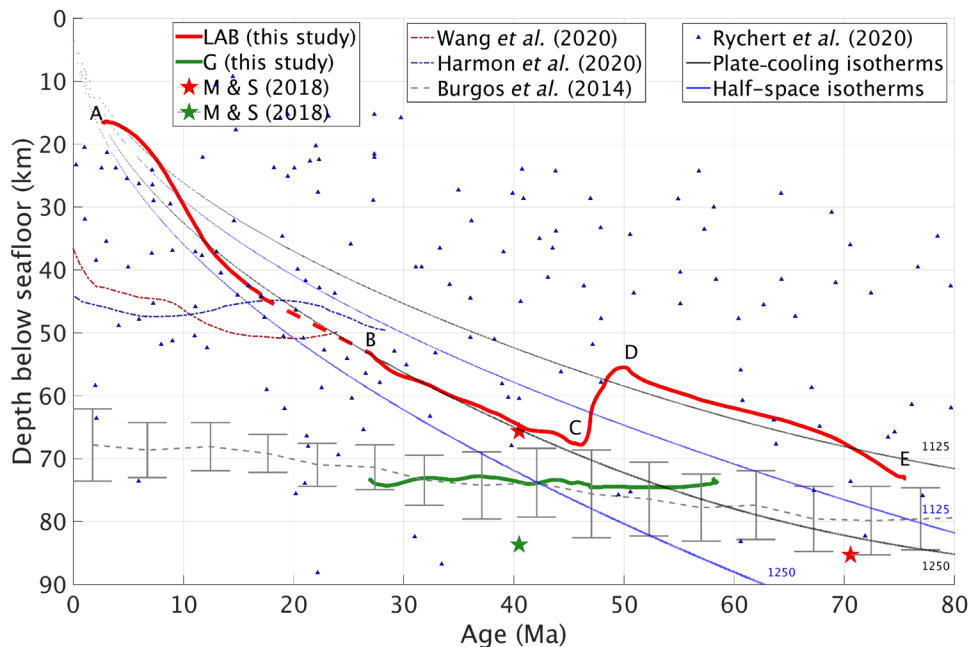

Fig. 3. Depth-converted image. Depth-converted mantle reflections, interpreted as the LAB (red) and G-reflection (green). Red dashed line indicates the interpolated depth from 16 Ma to 27 Ma. Best-fitting half-space (solid blue) and plate-cooling (solid black) isotherms are also plotted (*1*, *53*) and have an uncertainty of ±20°C (fig. S25). Results from seismic reflection study across the St. Paul fracture zone are shown by red (top) and green (bottom) stars at 40 Ma and 70 Ma, respectively (*13*). Dashed gray line with error bars indicates the results from radial anisotropy in the Atlantic Ocean (*3*). The blue triangles indicate the ensemble of LAB depths observed from previous studies (*10*) showing widespread LAB depths. Recent results from surface wave tomography (solid dotted blue line) (*4*) and colocated magnetotelluric experiment (solid dotted brown line) (*29*) just south of Chain fracture zone have also been plotted. The surface wave tomography and magnetotelluric results have a depth uncertainty of ≥10 to 15 km (*4*, *29*).

the ridge axis (Fig. 4), which could extend up to 5 Ma (*19*). Between 12 and 47 Ma, the LAB reflection seems to follow the 1250 ± 20°C isotherm of the plate-cooling model (*1*) with a slope of 1 km/Ma (fig. S24), which is close to the estimated 1260°C isotherm observed for the 40-Ma and 70-Ma-old lithosphere by Mehouachi and Singh (*13*). The depth of the LAB smoothly increases with age from ~53 km at 27 Ma (point B) to 67 km at 47 Ma (point C).

The isochrone line C-D shows that the LAB shallows from ~67 km at point C to ~55 km at point D (Fig. 3). As seen in the seismic image (Fig. 2 and fig. S19), this shallowing of the LAB happens in two distinct steps and correlates very well with the intersection of the two SODs with the seismic profile (fig. S1; red shaded regions in fig. S19).

Thermal rejuvenation

The LAB along the oldest part of the profile (D-E), south of the discontinuities, is observed at ~55 km (49 Ma) continuously deepening with age to 73-km depth at 75 Ma (Fig. 3), suggesting that the LAB in this age range is ~14 km shallower than that observed along profile B-C over 27 Ma to 47 Ma, but has nearly the same dip (1 km/Ma; fig. S24). Mehouachi and Singh (*13*) have observed shallowing of the LAB by 12 km over the 30-km distance across the St. Paul fracture zone, with the age contrast of 30 Ma, indicating that a strong thermal gradient could persist across discontinuities at older ages. The cross-correlation of the LAB reflections between 49 Ma to 75 Ma and 27 Ma to 47 Ma suggests that the lithosphere between 49 Ma and 75 Ma might be thermally rejuvenated by ~20 Ma (see fig. S26 and Materials and Methods). This estimate is very close to the age difference between the volcanic outcrops of the St. Helena volcanic chain and the surrounding seafloor [Fig. 1; (*14*)], which supports the interpretation that the rejuvenation of the LAB is linked to the passage of the St. Helena plume 50 Ma to 80 Ma ago.

Thermal rejuvenation due to impingement of plume material at the base of the lithosphere (*20*) and subsequent shallowing of the LAB (*21*) has also been observed for the Hawaii (*22*) and Reunion (*23*) plumes. However, the presence of the young volcanic chain, CVL, could also introduce a mantle thermal anomaly beneath this part of the lithosphere by the oceanward propagation of plume material (*24*) and rejuvenating the lithosphere (Fig. 4). If the lithosphere in this area is thermally rejuvenated and the ~1250°C isotherm demarcates the LAB as suggested for the 12-Ma to 47-Ma lithosphere (Fig. 3), then the ambient mantle temperature along this part of the profile should be relatively hotter, e.g., by ~160°C (fig. S27), than normal ambient mantle temperature. In other words, the ambient mantle temperature would be 1570°C instead of the 1410°C assumed for the normal mantle temperature (*25*) to uplift the estimated ~1125°C isotherm to the required ~1250°C at the LAB (see Materials and Methods and fig. S27).

Further evidence of a thermal anomaly affecting the oldest part of the profile (D-E) comes from the analysis of the basement topography (fig. S28, A and B) along the profile, which is about 570 m shallower than predicted by the subsidence models (see Materials and Methods). To explain this uplift in the basement topography, a mean excess temperature of ~115°C is required in the asthenospheric mantle (see Materials and Methods and fig. S28C), supporting the rejuvenation interpretation. On the basis of a seismological study, an excess temperature of 280°C from a depth of ~50 km extending down to at least 300 km has been estimated beneath the present-day hotspot of the CVL (*24*). Hence, it is possible that the mantle thermal anomaly from the CVL extends to the oldest part of our profile by a large-scale asthenospheric flow (Fig. 4) as has been proposed between the La Reunion Island and the Central Indian Ridge (*26*). We further computed the regional excess temperature from the basement uplift (*14, 27*) and found that our
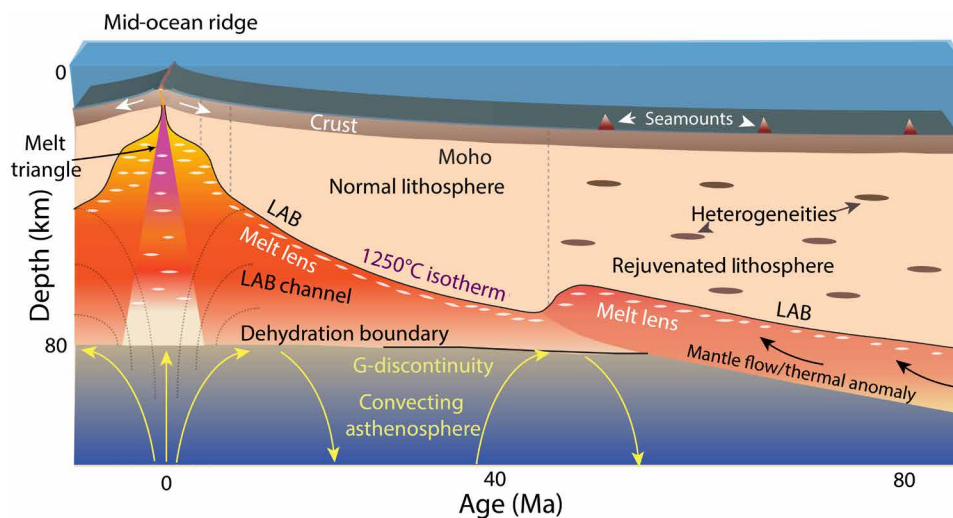

Fig. 4. Schematic diagram of the LAB and G-reflections. Schematic diagram showing the final interpretation as a function of age. The depth and age are approximate. The triangle beneath the ridge axis is the melt triangle. The LAB is marked by a solid black line following the 1250 ± 20°C isotherm for the lithospheric ages >12 Ma. The black dashed vertical lines indicate the change in the dip of the LAB at 5 Ma, 12 Ma, and 47 Ma. For ages >47 Ma, the lithosphere is possibly thermally rejuvenated caused by the St. Helena and/or Cameroon plumes. The white horizontal ellipsoids represent melt lenses at the LAB. The G-reflection (horizontal black line) denotes the Gutenberg discontinuity, interpreted as a dehydration boundary formed at the ridge axis (*36*) separating the primitive mantle beneath from the depleted mantle above. Light gray arrows indicate the flow beneath the ridge axis in the dry melting zone, and the yellow arrows indicate the mantle flow below the G-discontinuity. The mantle thermal anomaly is indicated for ages >50 Ma, with curved black arrows indicating direction of mantle flow. The mantle thermal anomaly could introduce heterogeneities in the lithosphere and produce seamounts on the seafloor.

profile lies on the edge of a large thermal anomaly in the asthenospheric mantle (see Materials and Methods and fig. S29). In conclusion, the shallow LAB reflection along profile D-E could be due to a combination of a thermal rejuvenation due to the impingement of the St. Helena plume and/or a thermal anomaly associated with the CVL.

Gutenberg discontinuity

The lower reflection lies at a constant depth of ~75 km and can be followed from 27 Ma to 58 Ma along the profile (Figs. 2 and 3); this depth is similar to the depths obtained from the radial anisotropy (Fig. 3) (3) and scattering studies (8) and has been interpreted as the G-discontinuity. The presence of a second deeper reflection has also been observed across the St. Paul fracture zone (13), where it has been interpreted as the base of a 17- and 12-km-thick melt channel at 40 Ma and 70 Ma, respectively. For a 120-Ma subducting lithosphere beneath the Northern Island of New Zealand, a ~10-km-thick channel is observed at 70- to 80-km depth (12). On the basis of a magnetotelluric (MT) study, a ~25-km-thick high-conductivity channel has been reported beneath the 23-Ma-old Cocos plate (28). A recent MT study from the equatorial Atlantic region shows a 10- to 15-km-thick high conductivity channel at a constant depth of 40 to 50 km for 0-Ma to 25-Ma-old lithosphere (29), in agreement with a colocated surface wave tomography study (Fig. 3) (4). However, the uncertainties in the MT and the surface wave results are in the range of 10 to 15 km (4, 29) and hence cannot be directly compared with our results. If our observed lower reflection corresponds to the base of a melt channel, the channel thickness would be 20 km at 27 Ma thinning to ~10 km at 40 Ma (Fig. 3), ~7 km thinner than that observed at 40 Ma further north (Fig. 3) (13). On the basis of a visual polarity study, Mehouachi and Singh (13) found that the lower reflection has a positive polarity, similar to the seafloor, requiring an increase in the velocity contrast, defining the base of the channel. However, our extensive polarity analysis (fig. S20) indicates that there is a high probability that the lower reflection has a negative polarity, requiring a ~5% decrease in the P-wave velocity at the interface (fig. S21B). The coincidence of the deeper reflection with the seismological results (3, 8) and the negative polarity suggest that the deeper reflection is associated with the G-discontinuity, which we call the G-reflection. It should be noted that the seismic reflection technique used here cannot distinguish if the reflection is produced by a thin (500 to 750 m) low-velocity layer or a step in the velocity at the interface proposed for the G-discontinuity (see fig. S22 and Materials and Methods) (3).

Melt beneath LAB

The deepening of the LAB along our profile with age indicates that it is primarily thermally controlled. Different mechanisms have been proposed to explain the presence of LAB (10, 11, 13). However, observations of widespread variations in the LAB depth with age (Fig. 3) have led to inconsistencies among the proposed mechanisms. To produce seismic reflection, a sharp P-wave velocity contrast is required, and the most plausible explanation would be the presence of melt (10, 13, 29, 30) at a freezing temperature as the temperature variation across the LAB would be very subtle. However, to retain melt at a subsolidus temperature, 1250 ± 20°C in our case, volatiles such as water or CO_2 would be required to lower the solidus temperature (31). Mehouachi and Singh (13) argue that the residual water from the melting cone enters the channel through a horizontal flux at the ridge axis (32). These buoyant partial melts

would ascend to the depths of the LAB where they are likely to be sheared into elongated horizontal bands due to stress-driven segregation of the lithospheric plate motion above (13) and possible self-sustaining small-scale convection (33) below. These elongated horizontal melt bands could produce a P-velocity drop sufficient to be imaged by the seismic reflection techniques. We find that ~1.1% of horizontal melt bands with an aspect ratio of 1:100 can explain the required velocity drop of 5.9 ± 0.6% at the LAB (see Materials and Methods and fig. S30), which is consistent with other estimates (1 to 1.5%) (3, 4, 12, 13). The amount of water needed to produce this volume of melt at the LAB would be in the range of 122 to 332 parts per million (ppm) (see Materials and Methods and fig. S31), which is also consistent with other estimates (10, 13).

Dehydration boundary

The depth of the G-reflection (~75 km) coincides with the base of the dry melting region beneath the ridge axis (34), suggesting that the G-reflection may represent a frozen-in boundary associated with the strong gradient in the water content beneath the ridge axis, separating the hydrated mantle below from the dehydrated mantle above. In the presence of such a dehydration boundary, strain can accumulate due to channel flow (35), resulting in a high strain gradient after 5 Ma to 10 Ma (6). Alternately, it has been suggested that the strong gradient in the water content beneath the ridge axis could form a 0.1- to 1-km-thick silicate melt layer at 70-km depth (11) that would freeze at older ages forming a gabbro sill and could produce the observed G-reflection. However, at younger ages (<60 Ma), such a gabbro sill would be molten at these depths, and the melt is likely to migrate upward to the base of the LAB, unless the layer between the G-discontinuity and the LAB is impermeable. Conversely, chemical studies have confirmed that the G-reflection is not caused by an attenuation contrast as suggested by some studies (36) but could be due to a depth-dependent increase in the amount of pyroxenite (37). However, the authors of this chemical study (37) themselves consider that the increase in pyroxenite is highly speculative in the absence of a plausible dynamical model.

The observed radial anisotropy at ~80-km depth could be produced by the strain induced by the differential relative motion between the depleted mantle above and the hydrated mantle below (5). Near the ridge axis, a high radial anisotropy extending from the depths of the G-reflection up to 150 km has been observed (36) and attributed to a zone of rapidly ascending melt (10, 30). On the other hand, the surface wave tomography results show that although the low S-wave velocities start around the LAB depth, they extend much deeper below the interpreted G-discontinuity (2) and have been attributed to be due to a melt-lubricated asthenosphere (38). Thus, the presence of low S-wave velocity below the LAB (2) would suggest the existence of partial melt between the LAB and G-reflection (13, 38), the G-discontinuity defining the base of LAB channel for young lithosphere (<50 Ma to 60 Ma). If the G-discontinuity is associated with a sharp decrease in velocity for younger lithosphere (7), then the G-discontinuity would represent a boundary between the LAB channel and the convecting asthenospheric mantle below. For older lithospheres, the top reflection might represent the G-discontinuity and the deeper reflection might represent the LAB. As the vertical separation between the LAB and G-discontinuity for older lithosphere would be <10 to 20 km, it would be difficult to distinguish them using low-resolution seismological methods, which might explain for different and sometimes conflicting results (8–10).

For a hot mantle, such as at the early stage of rifting (39) or ridge influence by a mantle plume, the melting will extend deeper and consequently the dehydration boundary would be deeper, and subsequently the corresponding G-reflection would be deeper as well. Once developed at the ridge axis (36), the G-discontinuity would be frozen and persist through all ages. However, in the presence of a thermal mantle anomaly and lithospheric rejuvenation, the G-discontinuity might get diffused and may disappear as observed in the older part of the profile (Fig. 2 and fig. S19).

LAB versus G-discontinuity

In conclusion, the LAB and G-discontinuity are two distinct boundaries, where the LAB is thermally controlled and possibly underlain by a melt channel. The LAB primarily deepens with age, consistent with thermal cooling models following the 1250°C isotherm, but factors such as mantle thermal anomaly also exert some control over the depth of its formation. On the other hand, the G-discontinuity represents a dehydration boundary (Fig. 4) formed at the ridge axis at a constant depth of ~75 km, separating the hydrated mantle beneath from the depleted mantle above. Both represent a sharp decrease in P-velocity, of the order of 5 to 6%, and cannot be distinguished at ages >40 Ma using conventional seismological methods. Above the LAB, ridge-push and slab-pull forces move the lithosphere, giving rise to plate tectonics. Between the LAB and the G-discontinuity, melt could exist in lower quantities and facilitate the movement of the lithospheric plate above. Below the G-discontinuity, mantle convection and large-scale mantle flows occur.

MATERIALS AND METHODS
Data acquisition

In 2015, we acquired a ~1400-km-long deep seismic reflection profile in the equatorial Atlantic Ocean onboard WesternGeco marine seismic vessel Western Trident. The profile was acquired along two flowlines from 1.8 Ma to 46.7 Ma (referred to as 2 Ma to 47 Ma for simplicity) and 49.3 Ma to 75.6 Ma (referred to as 49 Ma to 75 Ma for simplicity) and one isochrone line joining them (Fig. 1). We were obliged to change the line locations because of the possible extension of the exclusive economic zone of the countries in the region. A 12-km-long Isometrix streamer (40) with multi-sensors recording pressure (P), vertical acceleration (A_z), and horizontal acceleration (A_x, A_y) at every 3.125 m was towed at 30-m water depth. The seismic source was composed of six subarrays, each carrying eight air guns, having a total volume of 167 liters deployed at 15-m water depth. The initial shot interval was 75 m, and the record length was 30 s, starting from point E in the east. The vessel turned slowly, 1° per minute, at points C and D so that continuous data could be recorded during the turns. At point B, at 27 Ma, the shot interval was reduced to 50 m to increase the fold, and hence, the record length was reduced to 20 s. The vertical gravity gradient (41) map of the study region (fig. S1) better highlights the short offset transform faults and nontransform offsets, which we label as SOD. An almost continuous seafloor age variation (14) is covered by the profile (fig. S2). The half-spreading rate (14) varies between 8 and 23 km/Ma along the profile with a mean of ~20 km/Ma (fig. S2).

Onboard data processing

The seismic data were first processed onboard, which included anomalous amplitude attenuation (fig. S3) and swell noise removal

while keeping low-frequency signals. Optimal deghosting (fig. S4) was then performed by summing the pressure (P) and vertical velocity (V_z) components to enhance the signal bandwidth (40). Shot-by-shot source signature variation was removed by calibrating the marine source and performing source signature debubble deconvolution, which sharpened the image (fig. S5). The data were then decimated to 12.5-m receiver spacing and resampled to 8 ms. After common midpoint (CMP) binning and velocity analysis, multiples were attenuated using a suite of multiple attenuation algorithms including the generalized surface-related multiple elimination (SRME) (fig. S6), the weighted least-squares Radon (fig. S7), and post-Radon isolating multiple algorithms (fig. S8).

In the SRME, multiples of shallower interfaces are modeled from the input data using an autoconvolution without taking into account the bathymetry and are subtracted from the real data using an adaptive least-squares filter (42). Figure S6 shows considerable attenuation of the first-order multiples of the seafloor around 13 s and the second-order multiples of the seafloor around 20 s after the application of SRME. The Radon demultiple technique exploits the difference between the moveout of a primary event and its multiple in a moveout corrected CMP gather. A high-resolution Radon transform was used to distinguish between the primary and its multiple in the tau-p (slowness-time) domain, which was achieved using a conventional Radon transform and a time-variant weighting scheme applied during the transform. An extensive velocity analysis was performed to choose the best possible velocity for the moveout correction. Figure S7 shows notable attenuation of the multiple energy of the seafloor around 14 and 22 s after the Radon demultiple, except at zero offset where the primary and multiple moveout difference is minimum. Even after the application of the SRME and weighted least-squares Radon demultiple removal, residual multiple energy was still found in the data especially at zero offsets where the difference between the primary and multiple energy moveout is minimum. In a last attempt to remove the residual multiple energy, post-Radon isolating multiple technique was applied, which uses spectral decomposition unlike previous techniques that relied on a velocity model. Figure S8 shows the first-order seafloor multiples around 13 to 14 s to have been substantially attenuated after the application of post-Radon demultiple.

Enhanced processing

As our target is very deep and the seafloor is rough, high-frequency energy gets attenuated, and hence, we require low-frequency signals to image the LAB. Since the streamer was deployed at 30-m water depth, the first notch due to seafloor ghost will be at 25 Hz (43), which enhanced the low-frequency energy. Therefore, the first step of the enhanced processing was band-pass filtering (1.5 to 5 Hz) and low-frequency boost-up in the 2- to 5-Hz bandwidth to enhance the deep reflections (fig. S9). The following steps were taken to enhance the weak signals.

Low-frequency enhancement

To enhance the low frequencies, a time-variant spectral balancing of seismic data was performed using a time-frequency decomposition, with Gabor-Morlet wavelets being used for wavelet transforms. The Gabor-Morlet wavelet transform [$G_j(t)$] (44) in the time domain (t) is denoted by

$$G_j(t) = e^{-a_j t^2} e^{i\omega_j t}$$

where $a_j = \frac{\log(2)\,\omega_j}{4\pi^2}$ and ω_j is the frequency of the jth wavelet. This can be written in the frequency domain (ω) as

$$G_j(\omega) = \int_{-\infty}^{+\infty} G_j\, e^{i\omega_j t}\, dt = \sqrt{\frac{\pi}{a_j}}\, e^{\frac{-(\omega-\omega_j)^2}{4a_j}}$$

The width of the jth wavelet in the time domain (Δt_j) and in the frequency domain ($\Delta\omega_j$) can be related to its frequency, ω_j, as

$$\Delta t = \frac{k_1}{\omega_j}$$

and $\Delta\omega_j = \frac{k_2}{\omega_j}$.

The values of k_1 and k_2 above can be found by approximating $e^{\frac{-a_j\Delta t_j^2}{4}} = \frac{1}{2}$ in the time domain or equivalently in the frequency domain, $e^{\frac{-\omega_j^2}{4}} = \frac{1}{2}$.

The above approximation gives $k_1 = 4\pi$ and $k_2 = \frac{2\log(2)}{\pi}$.

We used the beginning and the central frequencies as 2 and 5 Hz, respectively, and divided the frequency interval into 12 smaller frequency bands to perform the low-frequency enhancement. The frequency spectra before and after the low-frequency enhancement show a boost in the energy around the dominant frequency of ~4 Hz (fig. S9).

Linear dipping noise removal

In the preprocessed shot gathers provided by WesternGeco, linear dipping noise was observed starting from both near offset and far offset dipping in opposite directions (positive and negative and highlighted by red windows in fig. S10A). The positive dipping noise was first flattened by a linear moveout correction using a velocity of 1800 m/s, which was then removed using a dip filter, followed by an inverse linear moveout correction. To remove the negative dipping noise, the offsets were flipped and then the noise was flattened by a linear moveout correction with a velocity of 2300 m/s. This was again removed by a dip filter, and an inverse linear moveout correction was applied followed by flipping back of the offsets to restore original shot gathers. Energies previously obscured have become much clearer as highlighted by the window in fig. S10B.

Offset interpolation and flat-events enhancement

To enhance the fold and signal-to-noise ratio (fig. S11A), an offset interpolation was performed in the CMP domain, decreasing the original trace spacing of 100 to 150 m in the CMP domain to 12.5 m. The interpolation was performed through a coherency analysis using windowed dip-based semblance. To estimate the dip of the mantle reflections as would be recorded by a 12-km-long streamer, we performed numerical modeling to compute synthetic seismograms (45) for both dipping and flat mantle reflections. We took the top mantle reflection at a 1300°C isotherm (46) and the bottom reflection as a relatively flat interface at ~90-km depth (fig. S12A). We chose the highest isotherm to have a maximum curvature for the top reflection for getting the best estimate of the dip. The top reflections represented a 10% P-velocity drop, and the bottom reflection represented a 10% P-velocity increase, bounding a melt channel (12, 13). The resulting dip of the reflection on seismic gathers was found to mostly flat within the range of 0.5 to 1 ms/m (fig. S12, B to E). For performing the interpolation, the semblance values were calculated via local slant stack for all traces in all dip directions within a window and smoothed for stability over a wavelet of size 120 ms, leading to a coherency function as a function of dip and time. The peak coherency values were found and interpolated to their exact dip values and sorted from largest to smallest. By examining the peak coherency value and its ratio over other picked coherencies, the number of dips contributing to the interpolation is determined. The time samples in the two nearest input traces were then used to interpolate along those selected dips to create an output sample value. This process was repeated sample by sample for each interpolated trace. This resulted in improved signal-to-noise ratio as can been seen in fig. S11B. Normal moveout (NMO) correction was then applied to the offset interpolated CMP gathers using the best possible velocity found by analyzing constant-velocity full-offset stacks. Figure S13 shows NMO-corrected gathers for four different velocities. It can be seen that the effect of stacking velocities is less for deeper events for stacking velocities >5 km/s. The best possible stacking velocities were found to be between 6 and 8 km/s. To further enhance the flat events, nonflat events were filtered out using a wave number filter after the NMO correction. The wave number filter enhances the energies along the zero wave number that correspond to flat events. The final CMP gather used for stacking after the wave number filter is shown in fig. S11C, and substantial improvement can be seen in the regions highlighted.

After the NMO correction and the wave number filter, we applied a mute function to stack only 0- to 4-km offset range for the seafloor and the Moho and the full offset range 0 to 12 km for the mantle reflections. Since the offset range used for stacking the mantle reflections is more than double than that used for the Moho, we obtain a better image of the mantle reflections. Furthermore, an image of a shallower reflection such as the Moho is more susceptible to seafloor/basement topography causing it to have a more variable dipping structure compared to the deeper reflections. It is this reduced variability in the structure of the mantle reflections, which we take advantage of in our processing scheme, that provides us a better image of the mantle reflections than the Moho.

Post-stack processing

Figure S14 shows seismic images after different stages of the processing. Figure S14A shows the seismic image after low-frequency enhancement (fig. S9) and linear noise removal (fig. S10). One can clearly see enhancement for some reflection events marked by red arrows. After the additional step of the offset interpolation and flat-events enhancement in the CMP domain, we observed further improvement in the reflection (fig. S14B). However, the reflection event is still not strong enough due to low signal-to-noise ratio. Hence, we performed a suite of post-stack processing steps to achieve further improvement as described below.

First, an iterative time-variant band-limited noise suppression was applied from 1 to 5 Hz, which decomposed the data into coherent and noncoherent signals (noise). The decomposition of the data is performed by a pass-band Butterworth filter $[A(f)^2]$ given by

$$A(f)^2 = \frac{1}{\left[1 + \left(\frac{f_{\text{beg}}}{f}\right)^{2N}\right]\left[1 + \left(\frac{f}{f_{\text{end}}}\right)^{2M}\right]}$$

where f_{beg} and f_{end} define the low and high cutoff frequencies of the noise component of the data and are taken as 1 and 10 Hz, respectively. N and M define the slopes of the filter on the low and high sides of the pass band and have been taken as 3 (18 dB/octave) and 6 (36 db/octave), respectively. After this decomposition, the envelopes of the signal and noise traces are calculated as a complex trace attribute. This complex trace attribute is essentially the sum of the trace with its Hilbert transform (90° phase rotated version). The

envelopes for signal and noise components of the data were smoothed over a 60-ms time window. The envelopes of the noise and signal traces are then compared, the time zones where the noise component exceeds the signal component are determined, and the amplitudes of the noise component in these time windows are scaled down to be similar to that of the signal components. Both the signal and scaled noise component data are then added to yield the final result.

Next, a windowed frequency-space deconvolution was performed iteratively to attenuate the diffraction tails. The window size was 3 km by 1.5 s, and the frequency range was 2 to 5 Hz. This window size was chosen after a trial-and-error method. The deconvolution essentially involves performing a Fourier transform to convert the data from the time domain to the frequency domain, which is then multiplexed with the offset domain to get the frequency-space series. Each of these frequency-space series is autocorrelated, and a prediction filter is designed using a complex Weiner inversion technique to eliminate the random part of the autocorrelation and enhance the predictable part of the signal. This prediction filter is then applied to the frequency-space series, which is then scaled and added to the original frequency-space series. Then, the demultiplexing of the frequency-space series to the frequency domain is performed followed by an inverse Fourier transform to the time domain.

Then, a dip-based windowed coherency search was performed and half of the maximum coherency energy was added back to the data to highlight the reflection. The coherent components of the input seismic data are estimated by their linear alignment over the windowed traces within a dip range. The linear alignment is computed by average cross-correlation, or coherence, between all pairs of traces within the window. This is performed for each dip within the range of 0.5 to 1 ms/m, corresponding to mostly flat events within the window. This yields coherency as a function of dips, and then up to three peaks in this coherence function are selected, each of which gives an interpolated value of dip together with the associated coherence. Any coherency peak less than a specified threshold (=1) is rejected, and the remaining coherency-dip peaks are stored within a wavelet obtained by averaging along the dip over the window. These coherency wavelets are then given a relative weight of 50% and added back to the original data.

Last, a windowed frequency–wave number (F-K) transformation of the data was performed and the amplitude of each sample in the F-K spectrum was squared without changing its phase. The resulting data are inverse transformed into the offset time domain and are repeated for the next window, which has 50% overlap with the previous window. For flat-dipping reflections, a larger window size (3 km) was chosen, whereas for curved-dipping reflections, a smaller window size (0.5 to 1 km) was chosen to make the reflection locally flat-dipping in the window. All these parameters, such as the window size, except for dip range, were extensively tested, and the best parameters were chosen. An appropriate trade-off between the computation time and the desired result were obtained. The best resulting image is shown in fig. S14C. Although there has been a significant improvement in the quality of the image, the noise is further attenuated by applying a smoothing filter as described below.

Edge-preserving smoothing

An edge-preserving smoothing filter (47) was performed in window sizes ranging from 1 km × 0.5 s to 5 km × 1 s with 50% overlap between adjacent windows. Dips corresponding to a particular reflection were specifically searched for maximum coherency within assigned windows. Each of the windows were further subdivided into subwindows. The energies within each of these subwindows are ranked in the order of their coherencies and are amplified by a cosine weight function, with the energy corresponding to the maximum coherency given the most weight. The squares of the amplitudes are used to remove the phase effect. We performed synthetic tests (fig. S15) to optimize the filter parameters and found that a filter performed best when a specific dip is searched for a specific reflection. The objective of the test is to recover a complex pattern (fig. S15A) masked by sufficient Gaussian noise (fig. S15B). When searching for a specific dip pattern (fig. S15C), the recovered image is better as compared to searching for a wide range of dipping patterns (fig. S15D). In regions where the dip of a reflection changes rapidly, such as near the ridge axis, the method is not very efficient. The final seismic image is shown in fig. S14D. The above processing scheme was applied to the entire profile to obtain the final seismic image (Fig. 2), and picked mantle reflections are shown in fig. S16. The blow-ups of the image along the three segments of the profile are shown in fig. S17 (2 Ma to 27 Ma), fig. S18 (27 Ma to 47 Ma), and fig. S19 (47 Ma to 75 Ma). Since our processing strategy depends on the dip of a reflection, we find that the image is better for reflections away from the ridge axis, where the variation in the dip is small (figs. S18 and S19).

Veracity of the reflections

To make sure that these reflections are not associated with reverberation in the water (multiples), we plotted multiple arrivals on the final picked image (fig. S16), which clearly shows that they are not associated with multiples. Given the continuity of the reflections, we did not find any bathymetric feature parallel to and all along the profile (Fig. 1 and fig. S1) that could map into the plane as sideswipes. There are several features, specially between 2-Ma and 27-Ma age range (fig. S17), which could be real or artificial features, and therefore, we have not interpreted them.

Polarity of the reflections

We first analyzed visually the polarity of the observed reflections (Fig. 2 and figs. S17 to S19) to determine whether the two reflections represent a drop or an increase in the acoustic impedance. However, the analysis was limited to few selected regions where the reflections were best observed and the results were not very clear. Hence, we performed a comprehensive statistical analysis along the entire profile to determine the polarity of the observed reflections. The seafloor reflection is taken as a reference, where there is an increase in velocity and where the maximum amplitude corresponds to a positive polarity. We carefully picked the two prominent mantle reflections with the maximum absolute amplitudes. Around these picks, we determined the polarity of the maximum absolute amplitude of the energy in a time window ranging from ±0.1 to ±0.4 s for each trace and determined the percentage of samples having a maximum negative amplitude. A total of 190,760 traces were analyzed for the polarity of upper mantle reflection, and a total of 112,620 traces were analyzed for the polarity of the lower reflection out of 224,170 traces along the whole profile. The trace spacing is 6.25 m. Figure S20A shows the statistics for the whole profile, and fig. S20B shows the statistics for the 27-Ma to 47-Ma section of the profile where the two reflections are most clearly visible. For smaller window sizes, the two reflections have dominantly (>60%) negative polarities. With the increasing window size, the percent of samples having maximum negative or positive amplitudes within the

window decreases toward 50%. Corresponding to a dominant frequency of 4 Hz (fig. S9), a time window of 0.25 s provides a good indication of the polarities of the two reflections, with the probability of >50% showing negative polarities, suggesting that there is a higher probability that both reflections are associated with a decrease in the velocity at interfaces. However, one must be careful as a thin layer can change the polarity of a reflection due to interference effect. Therefore, we interpret both possibilities for the second reflection, but using other supports, especially the anisotropy, leads us to interpret this reflection to be associated with a decrease in velocity.

Amplitude of the reflections
We use a method to determine the amplitude of the mantle reflections (13, 18) in which we compare the observed amplitude of the target reflection with a reference reflection. We took the seafloor as the reference reflection and picked the maximum positive amplitude within a ±0.2-s window. Then, we picked both the maximum positive and negative amplitudes within ±0.2 s from the two mantle reflections (Fig. 2 and fig. S17 to S19). The picked mantle reflection amplitudes were corrected for the spherical divergence and the Earth's intrinsic attenuation given by

$$\frac{A}{A_0} = e^{\frac{-\pi f t}{Q}}$$

where A/A_0 is the seismic amplitude after/before attenuation, Q is the quality factor, f is the dominant frequency (fig. S9), and t is the two-way time (Fig. 2 and figs. S17 to S19). Given the wide range of Q values in the lithosphere, typically 80 to 1000 (11), we choose Q as 600.

After correcting the amplitudes of the mantle reflections, we computed the reflection coefficient of the seafloor reflection assuming normal incidence, defined by

$$R = \frac{\rho_2 v_2 - \rho_1 v_1}{\rho_2 v_2 + \rho_1 v_1}$$

where the densities and the P-velocities in the two media separated by the reflection interface are represented by ρ_1, ρ_2 and v_1, v_2, respectively. For the seafloor, the two media represent the water column in medium 1 and the uncompacted sediments in medium 2. We took ρ_1 and ρ_2 as 1030 and 1350 kg/m³ and v_1 and v_2 as 1500 and 1565 m/s, respectively (48). With the corrected amplitude of the upper mantle reflection (A_{upper}), the seafloor reflection (A_{sf}), and the seafloor reflection coefficient R_{sf} obtained above, the reflection coefficient at the upper mantle reflection (R_{upper}) can be computed as

$$R_{upper} = \frac{A_{upper}}{A_{sf}} \frac{R_{sf}}{(1 - R_{sf})^2}$$

considering only the seafloor and upper mantle reflection as the reflecting interfaces. Similarly for the corrected lower reflection amplitude (A_{lower}), we get

$$R_{lower} = \frac{A_{lower}}{A_{sf}} \frac{R_{sf}}{(1 - R_{sf})^2} \frac{1}{(1 - R_{upper})^2}$$

considering the seafloor and the upper and lower mantle reflections as the reflecting interfaces.

For the upper and lower mantle reflections, we assumed that the mantle density remains constant at 3300 kg/m³ (49), reducing the reflection coefficients (R_{upper}, R_{lower}) to the ratio of change in velocities. We used this ratio to compute the upper limit of the percent P-velocity change across the upper and lower mantle reflections (fig. S21)

$$\delta v_P(\%) = 200 \frac{R_{upper/lower}}{1 - R_{upper/lower}}$$

The same number of traces as for the polarity analysis (fig. S20) has been taken for the reflection coefficient estimation for both the upper and lower reflections. A best-fitting log-normal curve (solid black curve in fig. S21) was obtained, and the modal value of the respective log-normal curves (black dashed vertical line in fig. S21) was taken as the percent P-velocity change for the upper (fig. S21A) and lower reflections (fig. S21B). The uncertainty was taken as one standard deviation (SD), typical for log-normal curves.

Synthetic seismogram modeling
We computed synthetic waveforms (45) to estimate the best 1D velocity models (fig. S22, A to C) that could yield the waveforms of the observed mantle reflections. The first model consists of sharp interfaces at the two mantle reflections with a constant velocity between them (fig. S22B). The second model consists of thin low-velocity layers at the depths of the mantle reflections. We varied the thickness of these low-velocity layers from 50 to 1000 m and found the maximum amplitudes of the waveforms when the layers are 500- to 750-m thick (fig. S22C). The P-velocity drop across the two mantle reflections was kept as 5.9 and 5%, respectively (fig. S21). A Ricker wavelet of dominant frequency 4 Hz (fig. S9) was used in the modeling. A comparison of the synthetic zero-offset waveforms with observed waveforms (fig. S22, D to G) shows that the observed waveforms have a complex reverberating waveform. The peaks and troughs of the observed waveforms have very similar amplitudes, which could be due to interfering noise and/or much more complex model.

Depth conversion of the reflections
To convert the observed mantle reflections in the seismic image from two-way time to depth, we used colocated wide-angle tomography results for the crust and upper mantle from 2 Ma to 27 Ma (50). To incorporate for thermal effects near the ridge axis, we considered two distinct age ranges from 2 Ma to 10 Ma and 10 Ma to 27 Ma of the tomography velocities. The mean 1D velocity profile of the averaged velocities from the two age ranges was used for depth-converting the upper reflection from 2 Ma to 27 Ma. Since most of the P-velocity evolution happens in the first ~10 Ma from the ridge axis, we used the averaged 1D velocity profile from 10 Ma to 27 Ma for depth-converting the upper reflection from 27 Ma to 75 Ma. The upper mantle P-velocities were linearly extrapolated using the same mantle gradient at the maximum depth of the upper reflection. For the lower reflection, the decrease of P-velocities by ~5.9% (fig. S21A) across the first reflection was taken into account at the appropriate depth of the reflection along the profile. The 1D velocity profiles were smoothed by a 2-km moving average window and are shown in fig. S23 (black curve: 2 Ma to 27 Ma; red curve: 27 Ma to 75 Ma).

To see the effect of mantle velocities on the depth of the reflections and compute the uncertainty, we computed analytically the

average mantle velocity (v_{avg}) from the minimum and maximum P-velocities in the mantle (v_{min}, v_{max}), using the lithospheric two-way time of the reflections as a constraint (Fig. 2). Assuming linearly increasing mantle velocities, the relation simplifies to

$$v_{avg} = \frac{v_{max} - v_{min}}{\log\left(\frac{v_{max}}{v_{min}}\right)}$$

Varying the minimum mantle velocities from 8 to 8.3 km/s (50) and the maximum mantle velocities from 8.4 to 8.6 km/s (51, 52) gives an average mantle velocity in the range of 8.2 to 8.35 km/s. In this range of average mantle velocity, we find that the depth of the reflection varies by a maximum of ±1.2 km in the oldest part of the profile where the reflections are deepest. Combined with the picking uncertainty of the reflections from the seismic time (Fig. 2 and figs. S17 to S19), we estimate the uncertainty in reflection depths to be ±3 km.

Figure S24 shows the variation of the dip of the depth-converted reflections with age. The maximum dip of the upper reflection is seen at ~10 Ma (2.5 km/Ma), and the negative gradient from C-D represents shallowing of the top reflection along the isochrone line.

Thermal modeling
Having obtained the depths of the age-dependent upper mantle reflection continuously from 2 Ma to 75 Ma (Fig. 3), we tested several plate-cooling (53) models to obtain a best-fit isotherm. The mantle potential temperature in the thermal modeling was taken as 1410°C (25), and the half-spreading rate was taken as the mean half-spreading rate over the profile of 20 km/Ma (14). The plate thickness and the thermal diffusivity were taken from the published model as 106 km and 6.7×10^{-7} m^2 s^{-1}, respectively (1). The best-fitting isotherms have been plotted in Fig. 3. The uncertainty in the fitting of the isotherm was obtained with respect to mantle potential temperature comparable to the LAB depth uncertainty of ±3 km and is ±20°C (fig. S25).

Thermal rejuvenation of 49-Ma to 75-Ma-old lithosphere
Cross-correlation of LAB depths
Observing similarities in the depths of the LAB reflections between 27 Ma to 47 Ma and 49 Ma to 75 Ma, we cross-correlated them (fig. S26A) to get the thermal rejuvenation and found the peak of the cross-correlation at ~20 Ma, suggesting that the 49-Ma to 75-Ma lithosphere might be rejuvenated by 20 Ma (fig. S26B). This estimate is of the same age difference between the St. Helena outcrops and the surrounding seafloor age in the study area [Fig. 1; (14, 15)], suggesting that the shallowing of the LAB might be due to the rejuvenation associated with the passage of the St. Helena plume.
Using higher mantle potential temperature
To explain the sudden shallowing of the LAB by ~14 km (Fig. 3), we recomputed the isotherms using the same plate-cooling model (1) but an elevated mantle potential temperature. Using higher mantle potential temperature (or hotter mantle) results in the shallowing of the isotherms (fig. S27), we found that the 1250°C isotherm in a hotter mantle (mantle potential temperature of 1570°C, red curve in fig. S27) is equivalent to the 1125°C isotherm of regular mantle (mantle potential temperature of 1410°C, black curve in fig. S27). For the profile D-E, this implies that either the LAB remains at 1250°C isotherm as for 12 Ma to 47 Ma (Fig. 3) but in a 160°C hotter mantle or it shallows to 1125°C isotherm if the mantle is unperturbed.

There is no scientific reason why the LAB would be at 1250°C isotherm along most of the profile and 1125°C for older ages, unless there are some thermal or chemical effects. We propose that the LAB lies at 1250°C isotherm all along the profile, but it has been rejuvenated either because of a thermal anomaly associated with the CVL or because of the passage of the St. Helena plume.

Basement uplift
The seafloor and basement topography for the whole profile were plotted with respect to the subsidence curves (fig. S28A) with the ridge-axis depth of 2655 ± 20 m at zero age, appropriate sediment velocities (54), and the parameters as in the above thermal model (1). The ridge-axis depth at zero age was obtained by best least-squares fitting of basement topography from 2 Ma to 47 Ma to the subsidence models (54). A zoom-in of the oldest part of the profile, D-E, is shown in fig. S28B, along with a sediment-unloaded basement interface. The sediment-unloaded basement (h_b) was computed by removing the sediment cover (h_s) from the basement topography (55)

$$h_b = h_s \frac{\rho_{sed} - \rho_{water}}{\rho_{mantle} - \rho_{water}}$$

where ρ_{sed}, ρ_{water}, and ρ_{mantle} are the densities of the sediment, water, and mantle, respectively (48, 49). The mean uplift of the sediment-unloaded basement with respect to subsidence curves is 570 ± 20 m.

We computed the excess temperature (δT) in the asthenospheric channel thickness (h) of 150 ± 50 km (56) required to produce an uplift (δU) using the relation (57)

$$\delta T = \delta U \frac{1 - \alpha T_m}{h\alpha}$$

where α is the thermal expansion coefficient in the mantle (1) and T_m is the mantle potential temperature (25). The required excess mantle temperature varies from 90°C at 49 Ma to 180°C at 74 Ma, with a mean excess mantle temperature of 115 ± 10°C (red shaded region in fig. S28C). These values are of the same order required for the rejuvenation of the lithosphere by 160°C.

We also extended the above calculations of basement uplift over a larger region to examine the nature of the underlying thermal anomaly, taking global bathymetry (14) and global sediment thickness (27). We observe that the oldest part of the profile, D-E, lies on the edge of a thermal anomaly (fig. S29).

Melt estimation at the LAB
We used effective medium theory (58) to compute the melt content from the P-wave velocities of the mantle peridotite. The background rock was assumed to be olivine-rich peridotite whose elastic parameters were taken from the literature (49). Melt is assumed to be present in thin horizontal lenses of aspect ratio 1:100 (12, 13) with appropriate elastic parameters (59). Figure S30 shows the effect of increasing inclusion of melt on the P-wave velocities of mantle peridotite for different aspect ratios. The curves become asymptotic beyond an aspect ratio value of 1:100. We used the percent P-wave velocity drop (fig. S21) on the P-wave velocities at the depth of the LAB reflection (fig. S23) to obtain the P-wave velocity just below the LAB (horizontal black dashed lines corresponding to 8 ± 0.05 km/s). This P-wave velocity corresponds to a melt fraction of 1.1 ± 0.1% (vertical black dashed lines) for thin horizontal lenses of aspect ratio 1:100 (fig. S30).

Water estimation for melt stability

Since the isotherms corresponding to the LAB depths (Fig. 3) are lower than the dry solidus of olivine, volatiles are needed to have melt below the LAB (*31*). The most common volatiles in the mantle are water and carbon dioxide, with water being as much as three times more effective than carbon dioxide in mantle melting (*60*). Since the concentration of carbon dioxide is not well constrained in the mantle (*60*), only the water concentration is considered and can be calculated by the relation (*31*)

$$F(P, T, X_{H_2O}^{bulk}) = \left[\frac{T - (T_{solidus} - \delta T(X_{H_2O}(X_{H_2O}^{bulk}, P, F)))}{T_{liquidus}^{lherz} - T_{solidus}} \right]^{\beta_1}$$

where F is the melt fraction expressed as a function of pressure, P, and temperature, T, at a given depth; $X_{H_2O}^{bulk}$ is the bulk water weight fraction in percent; X_{H_2O} is the relative water weight fraction in the melt; $T_{solidus}$ is the dry solidus temperature of olivine (blue solid curve in fig. S31); $T_{liquidus}^{lherz}$ is the lherzolite liquidus temperature (magenta solid curve in fig. S31); $\delta T(X_{H_2O})$ is the temperature decrease of the solidus due to X_{H_2O} in the melt; and β_1 is the power-law exponent of melt production. These various parameters along with their values have been detailed in the literature (*31*).

Taking the melt fraction, F, as ~1.1% (fig. S30), we estimated different $X_{H_2O}^{bulk}$ (red and green solid curves in fig. S31) at the pressure and temperature corresponding to the depths of the observed LAB reflections (horizontal black dashed lines in fig. S31). The estimated water content ranges from 122 to 332 ppm and can be considered as an upper limit.

SUPPLEMENTARY MATERIALS

Supplementary material for this article is available at https://science.org/doi/10.1126/sciadv.abn5404

REFERENCES AND NOTES

1. D. McKenzie, J. Jackson, K. Priestley, Thermal structure of oceanic and continental lithosphere. *Earth Planet. Sci. Lett.* **233**, 337–349 (2005).
2. K. Priestley, D. McKenzie, The thermal structure of the lithosphere from shear wave velocities. *Earth Planet. Sci. Lett.* **244**, 285–301 (2006).
3. G. Burgos, J.-P. Montagner, E. Beucler, Y. Capdeville, A. Mocquet, M. Drilleau, Oceanic lithosphere-asthenosphere boundary from surface wave dispersion data. *J. Geophys. Res. Solid Earth* **119**, 1079–1093 (2014).
4. N. Harmon, C. A. Rychert, J. M. Kendall, M. Agius, P. Bogiatzis, S. Tharimena, Evolution of the oceanic lithosphere in the equatorial atlantic from rayleigh wave tomography, evidence for small-scale convection from the PI-LAB experiment. *Geochem. Geophys. Geosystems* **21**, e2020GC009174 (2020).
5. N. Schmerr, The Gutenberg discontinuity: Melt at the lithosphere-asthenosphere boundary. *Science* **335**, 1480–1483 (2012).
6. H. F. Mark, J. A. Collins, D. Lizarralde, G. Hirth, J. B. Gaherty, R. L. Evans, M. D. Behn, Constraints on the depth, thickness, and strength of the G discontinuity in the Central Pacific from S receiver functions. *J. Geophys. Res. Solid Earth* **126**, e2019JB019256 (2021).
7. B. Gutenberg, On the layer of relatively low wave velocity at a depth of about 80 kilometers. *Bull. Seismol. Soc. Am.* **38**, 121–148 (1948).
8. C. Beghein, K. Yuan, N. Schmerr, Z. Xing, Changes in seismic anisotropy shed light on the nature of the Gutenberg discontinuity. *Science* **343**, 1237–1240 (2014).
9. L. Auer, T. W. Becker, L. Boschi, N. Schmerr, Thermal structure, radial anisotropy, and dynamics of oceanic boundary layers. *Geophys. Res. Lett.* **42**, 9740–9749 (2015).
10. C. A. Rychert, N. Harmon, S. Constable, S. Wang, The nature of the lithosphere-asthenosphere boundary. *J. Geophys. Res. Solid Earth* **125**, e2018JB016463 (2020).
11. S.-i. Karato, On the origin of the asthenosphere. *Earth Planet. Sci. Lett.* **321**, 95–103 (2012).
12. T. A. Stern, S. A. Henrys, D. Okaya, J. N. Louie, M. K. Savage, S. H. Lamb, H. P. Sato, R. Sutherland, T. Iwasaki, A seismic reflection image for the base of a tectonic plate. *Nature* **518**, 85–88 (2015).
13. F. Mehouachi, S. C. Singh, Water-rich sub-lithospheric melt channel in the equatorial Atlantic Ocean. *Nat. Geosci.* **11**, 65–69 (2018).
14. R. D. Müller, M. Sdrolias, C. Gaina, W. R. Roest, Age, spreading rates, and spreading asymmetry of the world's ocean crust. *Geochem. Geophys. Geosyst.* **9**, Q04006 (2008).
15. J. M. O'Connor, A. P. le Roex, South Atlantic hot spot-plume systems: 1. Distribution of volcanism in time and space. *Earth Planet. Sci. Lett.* **113**, 343–364 (1992).
16. J. Fitton, H. Dunlop, The Cameroon line, West Africa, and its bearing on the origin of oceanic and continental alkali basalt. *Earth Planet. Sci. Lett.* **72**, 23–38 (1985).
17. C. Wang, S. Song, C. Wei, L. Su, M. B. Allen, Y. Niu, X.-H. Li, J. Dong, Palaeoarchaean deep mantle heterogeneity recorded by enriched plume remnants. *Nat. Geosci.* **12**, 672–678 (2019).
18. Y. Qin, S. C. Singh, I. Grevemeyer, M. Marjanović, W. R. Buck, Discovery of flat seismic reflections in the mantle beneath the young Juan de Fuca Plate. *Nat. Commun.* **11**, 1–12 (2020).
19. The Melt Seismic Team, Imaging the deep seismic structure beneath a mid-ocean ridge: The MELT experiment. *Science* **280**, 1215–1218 (1998).
20. R. S. Detrick, S. T. Crough, Island subsidence, hot spots, and lithospheric thinning. *J. Geophys. Res. Solid Earth* **83**, 1236–1244 (1978).
21. C. Thoraval, A. Tommasi, M.-P. Doin, Plume-lithosphere interaction beneath a fast moving plate. *Geophys. Res. Lett.* **33**, 1–4 (2006).
22. X. Li, R. Kind, X. Yuan, I. Wölbern, W. Hanka, Rejuvenation of the lithosphere by the Hawaiian plume. *Nature* **427**, 827–829 (2004).
23. A. Bonneville, R. P. Von Herzen, F. Lucazeau, Heat flow over Reunion hot spot track: Additional evidence for thermal rejuvenation of oceanic lithosphere. *J. Geophys. Res. Solid Earth* **102**, 22731–22747 (1997).
24. M. M. Reusch, A. A. Nyblade, D. Wiens, P. J. Shore, A. Bekoa, C. Tabod, J. M. Nnange, Upper mantle structure beneath Cameroon from body wave tomography and the origin of the Cameroon volcanic line. *Geochem. Geophys. Geosyst.* **11**, 1–17 (2010).
25. E. Sarafian, G. A. Gaetani, E. H. Hauri, A. R. Sarafian, Experimental constraints on the damp peridotite solidus and oceanic mantle potential temperature. *Science* **355**, 942–945 (2017).
26. G. Baruol, K. Sigloch, J.-R. Scholz, A. Mazzullo, E. Stutzmann, J.-P. Montagner, S. Kiselev, F. Fontaine, L. Michon, C. Deplus, J. Dyment, Large-scale flow of Indian ocean asthenosphere driven by Réunion plume. *Nat. Geosci.* **12**, 1043–1049 (2019).
27. E. O. Straume, C. Gaina, S. Medvedev, K. Hochmuth, K. Gohl, J. M. Whittaker, R. Abdul Fattah, J. C. Doornenbal, J. R. Hopper, GlobSed: Updated total sediment thickness in the world's oceans. *Geochem. Geophys. Geosyst.* **20**, 1756–1772 (2019).
28. S. Naif, K. Key, S. Constable, R. Evans, Melt-rich channel observed at the lithosphere–asthenosphere boundary. *Nature* **495**, 356–359 (2013).
29. S. Wang, S. Constable, C. A. Rychert, N. Harmon, A Lithosphere-asthenosphere boundary and partial melt estimated using marine magnetotelluric data at the central middle atlantic ridge. *Geochem. Geophys. Geosyst.* **21**, e2020GC009177 (2020).
30. T. Sakamaki, A. Suzuki, E. Ohtani, H. Terasaki, S. Urakawa, Y. Katayama, K.-i. Funakoshi, Y. Wang, J. W. Hernlund, M. D. Ballmer, Ponded melt at the boundary between the lithosphere and asthenosphere. *Nat. Geosci.* **6**, 1041–1044 (2013).
31. R. F. Katz, M. Spiegelman, C. H. Langmuir, A new parameterization of hydrous mantle melting. *Geochem. Geophys. Geosyst.* **4**, 1–19 (2003).
32. T. Keller, R. F. Katz, The role of volatiles in reactive melt transport in the asthenosphere. *J. Petrol.* **57**, 1073–1108 (2016).
33. N. Harmon, D. W. Forsyth, D. S. Scheirer, Analysis of gravity and topography in the GLIMPSE study region: Isostatic compensation and uplift of the Sojourn and Hotu Matua Ridge systems. *J. Geophys. Res. Solid Earth* **111**, B11406 (2006).
34. G. Hirth, D. L. Kohlstedt, Water in the oceanic upper mantle—Implications for rheology, melt extraction and the evolution of the lithosphere. *Earth Planet. Sci. Lett.* **144**, 93–108 (1996).
35. D. B. Mark, G. Hirth, J. R. Elsenbeck, Implications of grain size evolution on the seismic structure of the oceanic upper mantle. *Earth Planet. Sci. Lett.* **282**, 178–189 (2009).
36. J. B. Gaherty, M. Kato, T. H. Jordan, Seismological structure of the upper mantle: A regional comparison of seismic layering. *Phys. Earth Planet. Inter.* **110**, 21–41 (1999).
37. L. Stixrude, C. Lithgow-Bertelloni, Mineralogy and elasticity of the oceanic upper mantle: Origin of the low-velocity zone. *J. Geophys. Res. Solid Earth* **110**, 1–16 (2005).
38. H. Kawakatsu, P. Kumar, Y. Takei, M. Shinohara, T. Kanazawa, E. Araki, K. Suyehiro, Seismic evidence for sharp lithosphere-asthenosphere boundaries of oceanic plates. *Science* **324**, 499–502 (2009).
39. H. Van Avendonk, K. J. Davis, L. J. Harding, A. L. Lawver, Decrease in oceanic crustal thickness since the breakup of Pangaea. *Nat. Geosci.* **10**, 58–61 (2017).
40. M. Vassallo, K. Eggenberger, D.-J. van Manen, A. Ozbek, P. Watterson, Broadband and beyond with marine towed streamers. *Lead. Edge* **32**, 1356–1365 (2013).
41. D. T. Sandwell, R. D. Müller, W. H. Smith, E. Garcia, R. Francis, New global marine gravity model from cryosat-2 and jason-1 reveals buried tectonic structure. *Science* **346**, 65–67 (2014).

42. R. Bisley, I. Moore, W. H. Dragoset Jr., Generalized 3d surface multiple prediction. U.S. Patent 7,796,467 (2010).

43. S. C. Singh, R. W. Hobbs, D. B. Snyder, Broadband receiver response from dual-streamer data and applications in deep reflection seismology. *Geophysics* **61**, 232–243 (1996).

44. J. Morlet, G. Arens, E. Fourgeau, D. Glard, Wave propagation and sampling theory—Part I: Complex signal and scattering in multilayered media. *Geophysics* **47**, 203–221 (1982).

45. R. M. Shipp, S. C. Singh, Two-dimensional full wavefield inversion of wide-aperture marine seismic streamer data. *Geophys. J. Int.* **151**, 325–344 (2002).

46. I. M. Artemieva, Global 1× 1 thermal model tc1 for the continental lithosphere: Implications for lithosphere secular evolution. *Tectonophysics* **416**, 245–277 (2006).

47. K. Bartyzel, Adaptive kuwahara filter. *Signal Image Video Process.* **10**, 663–670 (2016).

48. W. F. Ruddiman, T. R. Janecek, Pliocene-Pleistocene biogenic and terrigenous fluxes at equatorial Atlantic Sites 662, 663, and 664. *Proc. Ocean Drill. Prog. Sci. Res.* **108**, 211–240 (1989).

49. G. A. Abers, B. R. Hacker, A MATLAB toolbox and Excel workbook for calculating the densities, seismic wave speeds, and major element composition of minerals and rocks at pressure and temperature. *Geochem. Geophys. Geosyst.* **17**, 616–624 (2016).

50. V. A. Vaddineni, S. C. Singh, I. Grevemeyer, P. Audhkhasi, C. Papenberg, Evolution of the crustal and upper mantle seismic structure from 0–27 Ma in the equatorial Atlantic Ocean at 2° 43'S. *J. Geophys. Res. Solid Earth* **126**, e2020JB021390 (2021).

51. M. E. Pasyanos, T. G. Masters, G. Laske, Z. Ma, Litho1.0: An updated crust and lithospheric model of the earth. *J. Geophys. Res. Solid Earth* **119**, 2153–2173 (2014).

52. A. Ohira, S. Kodaira, G. F. Moore, M. Yamashita, T. Fujiwara, Y. Kaiho, S. Miura, G. Fujie, Active-source seismic survey on the northeastern Hawaiian arch: Insights into crustal structure and mantle reflectors. *Earth Planets Space* **70**, 1–16 (2018).

53. D. Hasterok, A heat flow based cooling model for tectonic plates. *Earth Planet. Sci. Lett.* **361**, 34–43 (2013).

54. P. Audhkhasi, S. C. Singh, Seismic structure of the upper crust from 0-75 ma in the equatorial Atlantic Ocean on the African plate using ultralong offset seismic data. *Geochem. Geophys. Geosyst.* **20**, 6140–6162 (2019).

55. C. Adam, V. Vidal, A. Bonneville, Mifil: A method to characterize seafloor swells with application to the south central pacific. *Geochem. Geophys. Geosyst.* **6**, (2005).

56. C. A. Dalton, C. H. Langmuir, A. Gale, Geophysical and geochemical evidence for deep temperature variations beneath mid-ocean ridges. *Science* **344**, 80–83 (2014).

57. R. A. Hartley, G. G. Roberts, N. White, C. Richardson, Transient convective uplift of an ancient buried landscape. *Nat. Geosci.* **4**, 562–565 (2011).

58. M. Taylor, S. C. Singh, Composition and microstructure of magma bodies from effective medium theory. *Geophys. J. Int.* **149**, 15–21 (2002).

59. A. N. Clark, C. E. Lesher, S. D. Jacobsen, Y. Wang, Anomalous density and elastic properties of basalt at high pressure: Reevaluating the effect of melt fraction on seismic velocity in the Earth's crust and upper mantle. *J. Geophys. Res.* **121**, 4232–4248 (2016).

60. M. M. Hirschmann, T. Tenner, C. Aubaud, A. Withers, Dehydration melting of nominally anhydrous mantle: The primacy of partitioning. *Phys. Earth Planet. Inter.* **176**, 54–68 (2009).